

# Observing sea ice flexural-gravity waves with ground-based radar interferometry

Dyre Oliver Dammann<sup>1,2</sup>, Mark A. Johnson<sup>3</sup>, Andrew R. Mahoney<sup>1</sup>, Emily R. Fedders<sup>1</sup>

<sup>1</sup>Geophysical Institute, University of Alaska Fairbanks, Fairbanks, Alaska, Fairbanks, AK 99775, USA

<sup>2</sup>Norwegian Geotechnical Institute, 0806 Oslo, Norway

<sup>3</sup>College of Fisheries and Ocean Sciences, University of Alaska Fairbanks, Fairbanks, AK 99775, USA

*Correspondence to:* Dyre Oliver Dammann (dyre.dammann@ngi.no)

**Abstract.** We investigate the application of ground-based radar interferometry for measuring flexural-gravity waves in sea ice. We deployed a Gamma Portable Radar Interferometer (GPRI) on top of a grounded iceberg surrounded by landfast sea ice near Utqiāġvik, Alaska. The GPRI collected 238 acquisitions in stare-mode during a period of moderate lateral ice motion during 23-24 Apr 2021. Individual 30-second interferograms exhibit ~20-50 s periodic motion indicative of propagating infragravity waves with ~1 mm amplitudes. Results include examples of onshore wave propagation at the speed predicted by the water depth and a possible edge wave along an ice discontinuity. Findings are supported through comparison with on-ice Ice Wave Rider (IWR) accelerometers and modeled wave propagation. These results suggest that the GPRI can be a valuable tool to track wave propagation through sea ice and possibly detect changes in such properties across variable ice conditions.

## 1 Introduction

Ocean waves play an important role impacting the formation, dynamics, and break-up of sea ice as established by numerous studies (Squire et al., 1995; Squire, 2007). Waves in sea ice have gained increasing attention in recent years due to rapid loss of sea ice in the Arctic (Yadav et al., 2020) leading to enhanced fetch. This is expected to increase ocean wave activity and the generation of swells which can penetrate far into the ice pack as flexural-gravity waves (Kohout et al., 2015). The propagation of infragravity waves through sea ice is complex as it depends upon resonant frequencies and can lead to leaky waves and edge waves along boundaries (Kovalev et al., 2020; Kovalev and Squire, 2020). Propagation of waves can in turn induce fracture, and break up ice floes into smaller pieces further accelerating sea ice decline (Thomson and Rogers, 2014).

The recognized significance of waves in ice and their dispersion and attenuation led to several advances in *in situ* and remote sensing methods as well as multiple scientific experiments conducted from drifting sea ice (Squire, 2018). Early assessments of wave propagation in sea ice were carried out using wire strain gauges (Squire, 1978) and used to detect “ice coupled” flexural-gravity waves in landfast sea ice (Crocker and Wadhams, 1988). Tilt meters were later utilized with easier deployment

**Deleted:** (Squire et al., 2021)

**Deleted:** ,

30 and maintenance (Czipott and Podney, 1989) partially through self-leveling mechanisms (Doble et al., 2006). Several other techniques have also proven valuable for wave detection in sea ice such as buoys, upward looking sonar (Thomson et al., 2019), and ship-based stereo imagery (Smith and Thomson, 2020).

Accelerometers are commonly utilized to measure waves in sea ice (Kohout et al., 2015; Sutherland and Rabault, 2016) and have significantly improved over the years (Doble et al., 2006) partly due to open source components (Rabault et al., 2020).

35 In this work, we utilize a system named Ice Wave Rider (IWR) which is based on the VN100 inertial measurement unit (IMU) manufactured by Vectornav Co. This system measures 3d acceleration at 10 Hz with a three-axis accelerometer and a three-axis gyroscope. The components are enclosed in a Pelican Storm Case and can be strapped down to the ice for 60-day deployments with Iridium telemetry of data (Johnson et al., 2020).

Remote sensing approaches have also been used to evaluate waves in sea ice such as lidar altimetry from ICESat2 to evaluate 40 waves in the marginal ice zone (Horvat et al., 2020). Synthetic aperture radar (SAR) has been used to estimate wave orbital velocity and wave height from backscatter distortion (Ardhuin et al., 2015; Ardhuin et al., 2017) and map wave fields through interferometry (Mahoney et al., 2016). These satellite-based approaches are valuable for evaluating waves in sea ice over large spatial scales, but are limited in temporal sampling. A higher sampling can be obtained with airborne systems (Sutherland et al., 2018), but logistics and cost can limit sampling to hours. For longer term observations of sea ice motion and deformation, 45 a ground-based system can be a more practicable solution. In recent studies, Dammann et al. (2021a) and Dammann et al. (in review) used a Gamma Portable Radar Interferometer (GPRI) to observe microscale horizontal strain and vertical motion of sea ice from installations on land, on a grounded iceberg surrounded by landfast sea ice, and from a pressure ridge in the drifting ice pack. From a suitable location on land, an instrument like the GPRI could be used to observe small-scale coastal sea ice motion indefinitely.

50 Here we demonstrate the application for monitoring mm-scale waves in landfast sea ice using data acquired by a GPRI while deployed on a grounded iceberg near Utqiáġvik, Alaska in April 2021. First, we model the expected results from idealized harmonic waves and compare with GPRI observations. Second, we compare observations with ice displacement data derived from three IWRs deployed on the ice. Finally, we discuss wave properties, accuracy, and limitations due to secondary vertical and horizontal motion.

## 55 2 Data and methods

### 2.1 Ground-based radar interferometry of sea ice

In this work, we utilize the Gamma Portable Radar Interferometer (GPRI). This coherent radar system is capable of detecting mm-scale displacements in sea ice through interferometry i.e., the assessment of the phase change,  $\Delta\Phi$ , in the radar backscatter over time (Dammann et al., 2021a).  $\Delta\Phi$  is proportional to the component of surface displacement aligned with the radar's line-

**Deleted:**

**Deleted:** (Schwendeman and Thomson, 2017)

of-sight (LOS), allowing relative horizontal displacement,  $d_{hr}$ , or relative vertical displacement,  $d_{vr}$ , to be calculated from the observed  $\Delta\Phi$  as follows:

$$d_{hr} = \frac{\Delta\Phi \lambda_s}{4\pi \sin \theta}, \quad d_{vr} = \frac{-\Delta\Phi \lambda_s}{4\pi \cos \theta} \quad (1,2)$$

65 depending on the signal wavelength,  $\lambda_s = 0.017 \text{ m}$  and incidence angle,  $\theta$ . For a GPRI system elevated above the ice surface, both horizontal and vertical motion can result in a significant LOS displacement (i.e., change in slant range) in the near field, within a few hundred meters of the GPRI. In this range, geometric constraints are required to resolve ambiguity between vertical and horizontal motions. Beyond such a distance, instrument sensitivity to vertical motion becomes negligible as incidence angle,  $\theta$ , approaches 90° and all phase change can be interpreted as horizontal.

70 The accuracy of the phase-derived ice motion depends on the interferometric coherence, a measure of how stable the reflected radar signal is over time, ranging between 0 (incoherent) and 1 (completely coherent). For points on the ice with high coherence, e.g., > 0.9, accuracy can reach sub-mm scale (Dammann et al., 2021a). However, accuracy can also be impacted by antenna movement (e.g., due to unstable GPRI footing) (Dammann et al., 2021a) or changing atmospheric conditions (Dammann et al., in review). The GPRI can be operated in either of two modes, scan mode, in which the antennas rotate while 75 acquired data, or stare mode, where an image is acquired while looking in a fixed orientation. Here, we apply the stare mode, in which the GPRI collects continuous measurements in one direction at 100 Hz. Individual observation timespans were limited to 30 s. During these sub-minute windows, we expect atmospheric contributions to be negligible.

In stare-mode, interferograms are oriented in range-time space where each row represents the phase change since the start of the acquisitions. Each row thus represents cumulative phase change up until a particular time and each column represents a 80 particular range point on the ice in the stare direction from the GPRI. We process all the interferograms by first averaging temporally to effectively reduce speckle and decrease the temporal sampling to 20 Hz. Then, we evaluate the progressive  $\Delta\Phi$  over 30 s and convert to vertical displacement according to Equation 1. We then subset the 30 s displacement timeseries to include only locations with high coherence (>0.999) and low variability (RMSE < 0.3-0.5 mm compared to a 1 s running mean).

## 85 2.2 Observations at Utqiāgvik

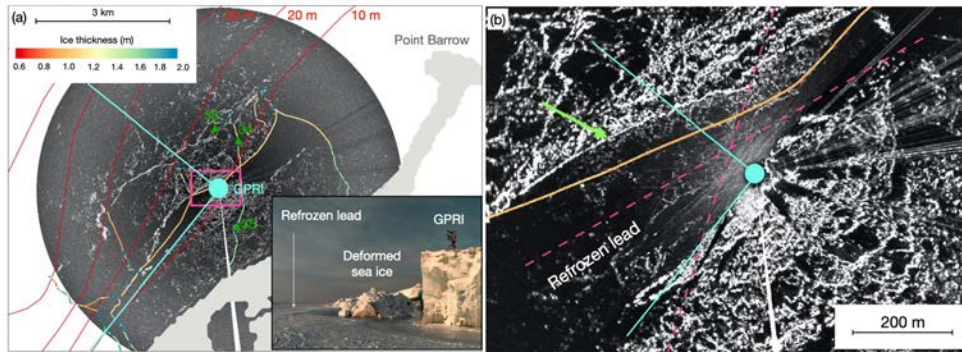
We carried out a series of observations on the landfast sea ice near Utqiāgvik during April-May 2021. The landfast ice consisted of first year sea ice and incorporated a large iceberg grounded at 10 m depth ~2 km offshore. We stationed a GPRI on top of the iceberg ~6 m above sea level (Figure 1a). The radar alternated between staring in a direction across and along a ~200 m wide refrozen lead (cyan lines in Figure 1b) every few minutes totaling 238 acquisitions. Within 200 m from the GPRI, we 90 expect the vertical sensitivity to be sufficient to pick up vertical motion. Clear wave signals were only identified in the stare direction across the lead possibly due to the smooth, uniform ice conditions. We also deployed three Ice Wave Riders (IWRs)

on the ice in the vicinity of the GPRI (green triangles in Figure 1a). These deployments enable a comparison between IWR- and GPRI-derived ice surface motion during only two across-lead acquisitions in which data overlapped (Table 1).

We evaluate ice thickness using measurements obtained between 16 Apr and 5 May 2021 as part of an annual community ice  
95 trail mapping project in Utqiāġvik. Ice thickness is derived from electromagnetic conductivity measurements obtained with  
snow machine pulling a GPS-equipped Geonics EM31-MK2 ground conductivity meter (Druckenmiller et al., 2013). Measurements were collected every second at speeds  $< 5 \text{ m s}^{-1}$  ensuring ice thickness measurements no more than 5 m apart. Ice thickness ranged from 0.6 m to several meter thick with areas of smooth ice being  $\sim 1 \text{ m}$  thick.

100 Table 1: Location and time of observations.

| Sensor | Start time<br>(UTC) | End time<br>(UTC) | Distance to<br>IWR 33 (km) | Distance to<br>GPRI (km) | Location (N,W)        |
|--------|---------------------|-------------------|----------------------------|--------------------------|-----------------------|
| GPRI   | 00:56 Apr 23        | 00:44 Apr 24      | 1.4                        | -                        | 71.361467, 156.630078 |
| IWR#33 | 00:19 Apr 24        | 01:05 May 26      | -                          | 1.4                      | 71.374531, 156.631160 |
| IWR#34 | 00:30 Apr 24        | 17:20 May 22      | 0.6                        | 1.2                      | 71.371703, 156.616030 |
| IWR#35 | 23:46 Apr 23        | 23:14 Jun 2       | 2.4                        | 1.0                      | 71.353681, 156.618920 |



105 Figure 1: (a) Location of the GPRI superimposed on scan-mode backscatter imagery. The GPRI stared in the directions of the cyan lines. Bathymetry contours are drawn in red. Location of IWRs is identified with green triangles. Multi-colored line shows ice thickness as indicated by the color bar. Land is masked out in light gray. The pink rectangle indicates the location of the zoomed-in panel in (b). (b) Zoomed in area of the refrozen lead adjacent to the GPRI. The pink dashed lines indicate possible directions of wave propagation commented on in the text. The green arrow in (b) indicates deformed offshore edge of the refrozen lead.

110 **2.3 Modeling wave dispersion and expected impact on stare-mode interferometry**

We model vertical ice displacement,  $d_v$ , in response to harmonic waves to investigate how the GPRI can be used to detect and characterize waves in sea ice:

$$d_v(x, t) = A \sin(kx - \omega t + \varphi_0) \quad (3)$$

Where  $A$  is the amplitude,  $x$  is the distance from the GPRI,  $k$  is the wavenumber ( $k = 2\pi/\lambda_w$  where  $\lambda_w$  is the wavelength of the propagating wave),  $\omega$  is the angular frequency ( $\omega = -2\pi/T$ , where  $T$  is the wave period),  $t$  is the time, and  $\varphi_0$  is the phase of the surface wave at  $t = 0$ . If the GPRI is placed on a fixed location e.g., the shore or firmly grounded ice, the vertical ice surface displacement relative to the GPRI,  $d_{vrfix}$ , will be equal and opposite the actual surface motion, that is:

$$d_{vrfix} = -d_v. \quad (4)$$

We can model interferograms by substituting  $d_{vrfix}$  for  $d_v$  in Equation 2. To demonstrate, we model waves in water depth,  $H$  = 10 m (based on bathymetric contours in Figure 1) and with period,  $T = 15$  s as an example. According to the shallow water approximation, the wave speed can be approximated to  $c \approx 9.9$  m s<sup>-1</sup> through the following expression based on gravity,  $g$ , and water depth,  $H$ :

$$c = \frac{\lambda_w}{T} \approx \sqrt{gH} \quad (5)$$

We obtained the same speed,  $c$ , using the full dispersion equation (Johnson et al., 2021) and ~1 m ice thickness based on the EM31 survey. Through  $c$ , we can also approximate  $\lambda_w = 150$  m for  $T = 15$  s. The resulting  $d_{vrfix}$  and associated interferogram is displayed in Figure 2a and b respectively.  $\Delta\Phi$  is most significant in near range due to the decreasing sensitivity of the GPRI to vertical motion with increasing range.  $\Delta\Phi$  exhibits a periodic, diagonal pattern where we can identify both the wave period and observed speed,  $c_o$ , based on the pattern spacing and angle respectively (Figure 2b).

The speed observed with the GPRI,  $c_o$ , may differ from the speed of the wave,  $c$ , and depends upon the angle,  $\alpha$ , between the GPRI line of sight (LOS) and the propagation direction of the wave i.e., if  $\alpha$  is non-zero,  $c_o$  will be greater than  $c$  because LOS distance between individual waves will be greater than the wavelength,  $\lambda_w$ . Hence, if waves propagate in LOS direction i.e.,  $\alpha = 0$ , then  $\lambda_o = \lambda_w$  resulting in  $c_o = c$ . However, if propagation direction approaches perpendicular to LOS, the observed distance in between wave crests,  $\lambda_o$ , approaches infinity along with  $c_o$ :

$$c_o = \frac{\lambda_w}{T \cos \alpha} = \frac{c}{\cos \alpha} \quad (6)$$

Incoming shallow water waves typically propagate perpendicular to bathymetric contour lines as wave speed decreases with decreasing depth (Equation 5). The LOS direction of the GPRI intersected the local isobaths approximately 15° from normal (Figure 1a), hence we expect to observe ~10 m s<sup>-1</sup> for waves propagating from offshore (modeled in Figure 2b). Inhomogeneities in the ice cover such as changing ice thickness, fractures, and rough ice can result in altered directionality of

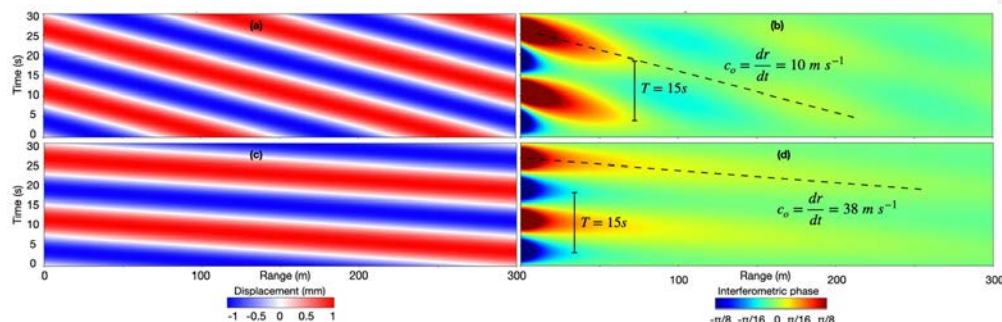
wave propagation. As an example,  $\alpha = 75$  is expected to result in  $c_o = 38 \text{ m s}^{-1}$  and the observed interferogram in Figure 2d.

140 If the GRI is placed on floating ice (subject to vertical and horizontal motion due to sensor uplift and tilt) the phase patterns will be more challenging to interpret. This is further discussed in the appendix.

The modeled example (Equation 3 and Figure 2) demonstrates a single wave field. In the case of a secondary wave field interfering, the superimposed waves can be expressed:

$$d_v(x, t) = 2A \sin(\bar{k}x - \bar{\omega}t) \cos\left(\frac{\Delta k}{2}x - \frac{\Delta \omega}{2}t\right) \quad (7)$$

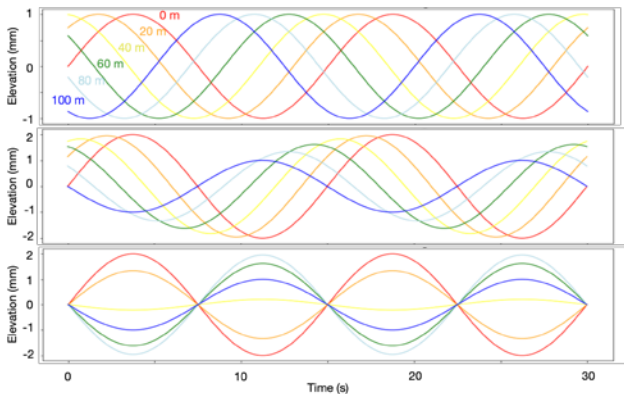
145 Where  $\bar{k}$  and  $\bar{\omega}$  represents average values of the two waves. The phase speed of the combined wave field, represented by the first term in Equation (7), is the average speed of the two waves. The second term is the wave envelope. Two wave fields can occur in sea ice when a reflected wave propagates along inhomogeneities such as cracks and ridges (e.g., edge waves) (Marchenko and Semenov, 1994; Marchenko, 1999) and interacts with the general wave field. Reflected waves have the same period and wavelength as the incident wave. However, the orientation of propagation relative to a GPRI stare line, and hence 150 also the apparent wavenumbers of the incident and reflected waves, will differ. From Equation 7, we get the resulting observed wave speed from individual waves  $c_{o1}$  and  $c_{o2}$  is  $\bar{c}_o = (c_{o1} + c_{o2})/2$ . As an example, we model a single wave field (Figure 3a) and superimpose an edge wave with  $c_{o2} = 2c_{o1}$  (Figure 3b) and reflected standing wave (Figure 3c).



155 Figure 2: (a) Relative vertical elevation (i.e., elevation difference between the GPRI and the ice surface) for simulated periodic oscillations in 10 m water depth ( $T = 15 \text{ s}$ ,  $A = 1 \text{ mm}$ ,  $\lambda_w = 150 \text{ m}$ ) for LOS parallel to wave propagation and (b) associated synthetic interferogram. Panels (c) and (d) show results for the same simulated oscillations but with a LOS at  $75^\circ$  to the direction of propagation. The phase magnitudes of the patterns in (b) and (d) will differ based on the elevation of the GPRI system above the ice surface (here 6 m).

160

Deleted: 6b  
 Deleted: s reflect off and  
 Deleted: Such r  
 Deleted: will have a similar  
 Deleted: and  
 Deleted:  
 Deleted: that is not normal to the crack,  
 Deleted: speed,  $c$ , as the incoming wave field, but with different observed speed  $c_o$   
 Deleted: Hence, f  
 Deleted: e  
 Deleted: observed  
 Deleted: W



175

**Figure 3:** Modeled vertical displacement in the GPRI stare direction at different positions in range in the case of (a) a single wave field with  $c_0 = 10 \text{ m s}^{-1}$ ,  $\lambda = 150 \text{ m}$ ,  $A = 1 \text{ mm}$  and  $T = 15 \text{ s}$ , (b) the wave field in (a) superimposed on a wave field with the same  $A$  and  $T$  as in (a), but  $c_0 = 20 \text{ m s}^{-1}$  and  $\lambda_0 = 300 \text{ m}$ , (c) a standing wave expected from an ideal reflection of the wave in (a).

#### 2.4 Deriving wave properties from Ice Wave Rider data

180 We interpret the vertical acceleration from the IWRs in the form of the power spectral density. This is derived by partitioning the acceleration time-series into 15-minute segments with a 50% overlap and smoothing twice in frequency with a 1-2-1 weighting. We then display the amplitude-frequency distribution over time in the form of Welch periodograms. This enables the identification of ubiquitous bursts of activity typically less than 15 minutes (see example in [Figure 4](#)). We can estimate the predominate direction of wave propagation from the cross-correlation lag time,  $l$ , in between the acceleration signals measured 185 at IWR#33 and IWR#34:

$$l = d \cos \psi / c \quad (8)$$

where  $d = 630 \text{ m}$  is the distance in between the IWRs and  $\psi$  is the propagation angle relative to the direct line in between the IWRs. We assume a similar wave speed as before of  $c = 9.9 \text{ m s}^{-1}$  as the ice in between the sensors was mostly smooth and estimated to  $\sim 1 \text{ m}$  thickness based on the nearby EM31 survey. A maximum correlation lag is thus expected to be  $l = 64 \text{ s}$  190 ( $\psi = 0$ ) and  $l = 63 \text{ s}$  for waves propagating directly onshore ( $\psi = 8^\circ$ ). We can derive the amplitude from the partitioned acceleration,  $a_z$ , as described by (Kohout et al., 2015) and further detailed in (Rabault et al., 2020):

$$A = a_z \omega^{-2} \quad (9)$$

We use a low frequency cutoff of  $T = 60 \text{ s}$ , double the acquisition window of the GPRI. Lower frequency waves will thus be difficult to detect within the 30 s GPRI window and will start to resemble uniform sea level change.

195

Formatted: Centered

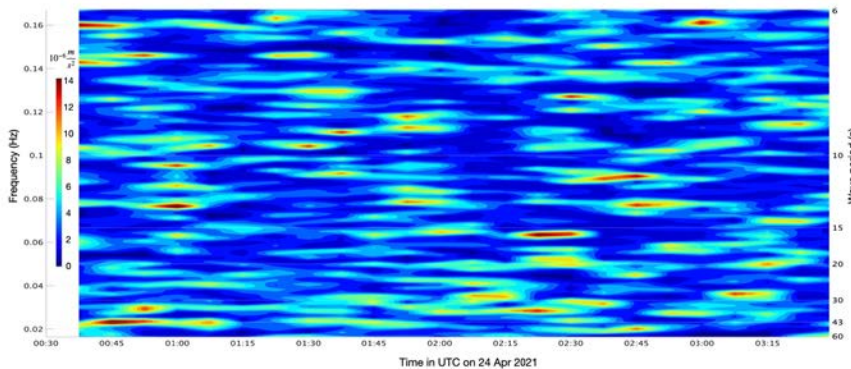
Formatted: Line spacing: single

Formatted: Font: 9 pt, Bold

Deleted: ¶

Deleted: Figure 3

Deleted: 7



200 **Figure 4:** Example of vertical acceleration measured by IWR#33 during the first ~3 hours after deployment on 24 April 2021. The acceleration is displayed as power spectral density in the frequency/time domain as a Welch periodogram. Numbers ranging from 6 to 60 to the right of the figure are period values in seconds corresponding with the frequency axis on the left-hand side

Deleted: Figure 3

### 3 Results

#### 205 3.1 Observing a single onshore wave field and comparison with modeled wave

A good example of a surface wave-like signal detected by the GPRI is the interferogram acquired on 23 April at 21:56 UTC (referred to as E1) where a negative  $\Delta\Phi$  signal (i.e., positive vertical displacement according to Equation 2) appears after the first ~15 seconds and propagates towards the GPRI over the last ~15 seconds (Figure 5a). To demonstrate the similarity with a wave signal, we model a wave according to Equation 3 from a fixed GPRI position. We model the wave with approximate 210 wave properties based on the observations ( $\lambda_w = 0.3 \text{ km}$ ,  $A = 0.9 \text{ mm}$ , and  $T = 30 \text{ s}$ ). The similarity of interferometric phase patterns between the observations and model (Figure 5a and 5b respectively) confirm that the GPRI did not tilt significantly during acquisition and can therefore be treated as a fixed deployment.

Deleted: an

Deleted: onshore wave

Deleted: Figure 4

Deleted: Figure 4

Deleted: 4

215 Additionally, we identify individual range points on the ice with high coherence, which exhibit wavelike oscillations in displacement over time (Figure 6a). For each such point, we identify the time of maximum displacement and use this to track the progression in the wave crest and derive the speed,  $c_o = 10 \text{ m s}^{-1}$  with a standard error of  $20 \text{ cm s}^{-1}$  (Figure 6b). The speed suggests that this wave likely propagated near directly onshore. The derived average amplitude for all high-coherence points is  $0.8 \pm 0.2 \text{ mm}$  (mean  $\pm$  standard deviation), which appears representative for the amplitude beyond 80 m from the GPRI (Figure 6c). However, as the wave approaches within 80 m of the GPRI, it increases slightly and then drops off closer than 35 m (dashed lines in Figure 6c).

Deleted: Figure 5

Deleted: -

Deleted: Figure 5

Deleted: (Table 2)

Deleted: Figure 5

Deleted: Figure 5

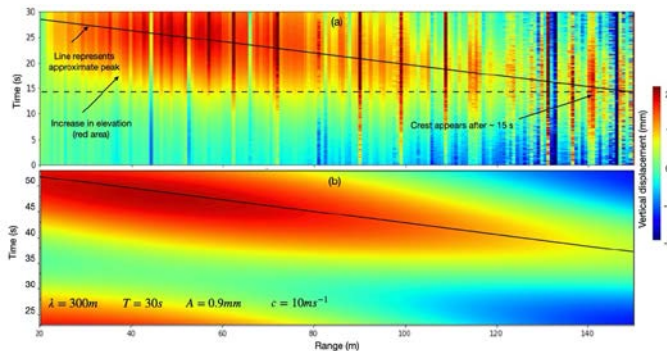


**Figure 5:** (a) Phase-derived vertical displacement over 30 seconds at 21:56 UTC. The displacement is displayed in the range-time space along one fixed direction. Transient features are thus expected to have a diagonal nature, where the angle represents the velocity of the feature. (b) Modeled displacement of a similar wave as in (a).

Deleted: Figure 4

235

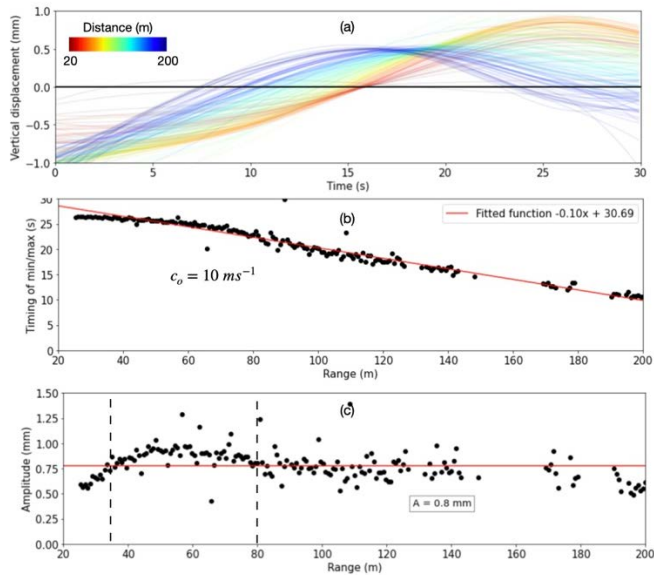
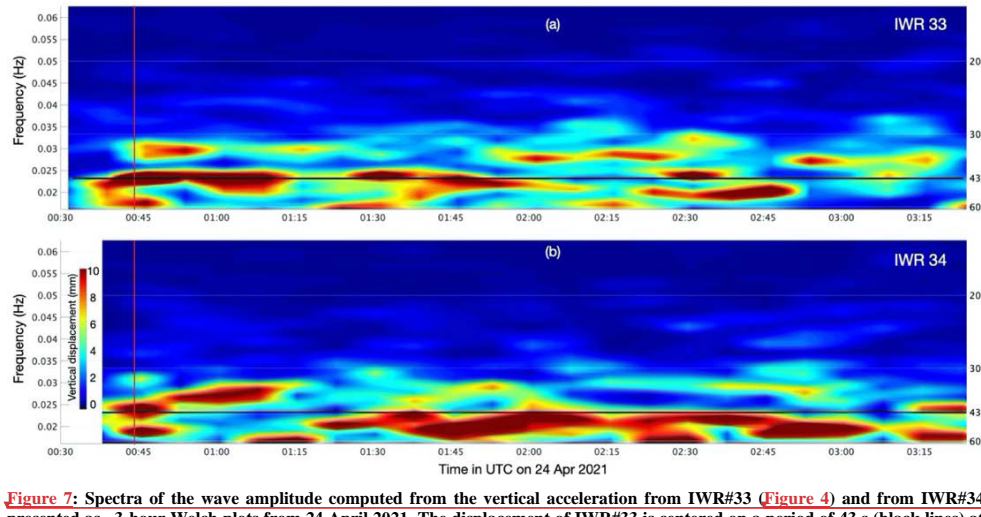


**Figure 6:** (a) Derived vertical displacement over 30 seconds on 23 April 2021 at 21:56 UTC (E1). Each line represents one location on the ice where warmer colors signify a closer distance to the radar. (b) Exact time of the wave crest at different distances from the radar. The linear fit indicates a wave velocity of  $10.0 \text{ m s}^{-1}$ . (c) Amplitude with range.

Deleted: Figure 5

### 3.2 Observing superimposed wave fields validated with data from Ice Wave Riders

The three Ice Wave Riders (IWR) were continuously operating from approximately 00:30 UTC on April 24 (Table 1) overlapping two GPRI acquisitions in the offshore direction. The derived vertical displacement is thus suitable for validation 245 of the GPRI data acquired at 00:32 and 00:44 UTC on 24 April. In this time window, we determine a cross-correlation lag time  $l = 63.5$  s in between IWRs indicative of predominately onshore wave propagation (Equation 8). We further evaluate the displacement spectral characteristics in the Welch periodograms (Figure 7). Wave amplitude relates to frequency according to Equation 9 resulting in the lower frequencies in Figure 4 dominating the displacement (Figure 7). The displacement exhibits energetic signals between 30 and 60 s, well within the wave band for flexural waves, which persist for less than an hour. Both 250 IWR#33 and IWR#34 suggest that several of the frequency peaks during and following the GPRI acquisitions (red line in Figure 7) are centered around 43 s (black lines in Figure 7). Although these peaks are small with an amplitude of  $\sim 1$  cm, they are significantly above the derived noise floor as indicated in Figure 8. IWR#35 is situated behind grounded ice, in shallower water with thicker ice and does not exhibit the same signal as the other IWRs.



255 **Figure 7:** Spectra of the wave amplitude computed from the vertical acceleration from IWR#33 (Figure 4) and from IWR#34 presented as  $\sim 3$ -hour Welch plots from 24 April 2021. The displacement of IWR#33 is centered on a period of 43 s (black lines) at 00:44 UTC (time indicated with red vertical line).

Deleted: Validating a GPRI-observed wave

Deleted: with

Deleted: Equation 7

Deleted: Figure 6

Deleted: Equation 8

Deleted: Figure 3

Deleted: Figure 6

Deleted: Figure 6

Deleted: Figure 6

Deleted:

Deleted: Figure 6

Deleted: Figure 3

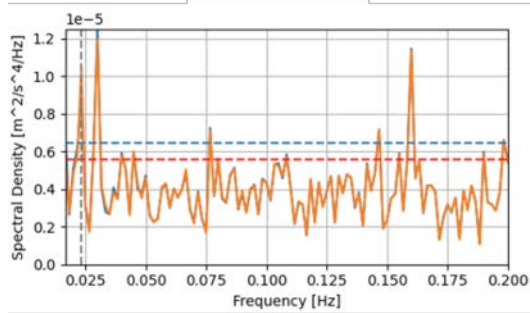


Figure 8: Solid lines indicate raw (blue) and band-pass filtered (orange) spectral density during the first hour of the IWR record. Dashed red line indicate the noise floor of the IMU sensor (from VectorNav data sheet). Dashed blue line indicates noise floor derived from the IWR when resting on the floor. The 43 s wave signal at ~0.025 Hz exceeds both of these noise floors.

Formatted: Normal

275

The last of the GPRI interferograms acquired at 00:44 UTC (referred to as E2) exhibits a clean wavelike motion (Figure 9a).

Deleted: Figure 7

We are able to track the timing of displacement maximum and minimums across most of the lead (Figure 9b) with a temporal

Deleted: Figure 7

lag of  $21.4 \pm 0.5$  s. The period is exactly double at  $T = 42.7 \pm 1.0$  s. This is the same as the peak displacement frequency

Deleted: identical

derived from IWR#33 (within measurement uncertainty) and suggests that the GPRI picks up the same wave field. The

Deleted: to

280

observed wave speed, derived from the slope of the maximum ice displacement (Figure 9b) is  $27 \text{ m s}^{-1}$  (with a standard error

Deleted: Figure 7

of  $25 \text{ cm s}^{-1}$ ) and larger than the speed of the incoming wave field at  $10 \text{ m s}^{-1}$ . We therefore assume that the observations

Formatted: Superscript

represent a reflected edge wave that can propagate along the lead superimposed on the incoming wave field identified with the

Deleted: (Marchenko, 1999)

IWRs. The actual speed of the two wave fields will be  $10 \text{ m s}^{-1}$ , but the observed speed of the edge wave  $c_{o2}$  needs to be

Deleted: (Marchenko, 1999)

considered. The reflected wave will have conserved period,  $T$ , and the same for the superimposed waves as demonstrated in

Deleted: Superscript

285

Figure 3b. As described by Equation 7,  $\bar{c}_o = (c_{o1} + c_{o2})/2 = 27 \text{ m s}^{-1}$  results in  $c_{o2} = 44 \text{ m s}^{-1}$  and suggests wave propagation

Deleted: Superscript

at  $\sim 76^\circ$  from the LOS. This is indicative of edge waves traveling directly up the refrozen lead (pink dashed line in Figure 1b).

Deleted: Superscript

In addition to waves reflecting at ice boundaries and traversing along leads and ridges at an angle, we expect the incoming

Deleted: Superscript

wave field to also be able to reflect directly off the iceberg with a conserved orientation. This is expected to lead to a standing

Deleted: a

wave as modeled in Figure 3c. A possible example of this was observed prior to the IWR data (Figure 10) where the minimum

Deleted: a

290

elevation of the trough occurs at  $\sim 15$  s out to a node of 100 m and beyond at  $\sim 27.5$  s, indicative of a standing wave with  $T \approx$

Deleted: a

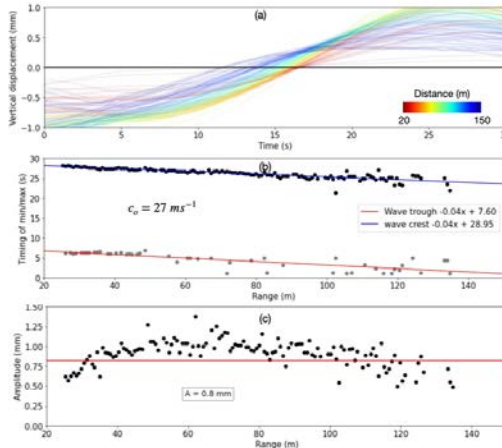
25 s. However, this signal bearing resemblance to a standing wave do not indicate more nodes (e.g., at  $\sim 300$  m) and incorporates

Deleted: a

a linear trend that was removed for the analysis (dashed line in Figure 10), possibly due to a simultaneous increase in water

Deleted: a

level.



305 **Figure 9:** (a) Derived vertical displacement over 30 seconds on 24 April 2021 at 00:44 UTC (E2). Each line represents one location on the ice where warmer colors signify a closer distance to the radar. (b) Exact time of the wave crest and troughs at different distances from the radar. The linear fit indicates a wave velocity of  $27 \text{ m s}^{-1}$  and period of 43 s. (c) Amplitude with range.

Deleted: Figure 7

## 4 Discussion

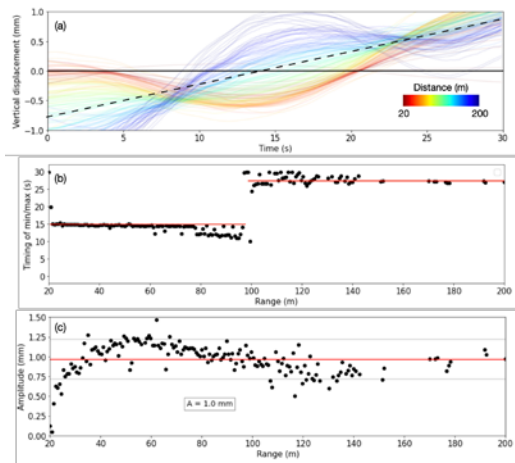
### 4.1 Interpreting wave amplitude and speed

310 The wave amplitudes derived from GPRI stare-mode observations approximately 3 hours apart (E1 and E2) are similar to each other and peaks at  $\sim 60\text{-}80 \text{ m}$  from the GPRI. Offshore from this distance, we attribute the increase in amplitude to shoaling as the water gets shallower. Closer than  $\sim 60 \text{ m}$  from the GPRI, the wave amplitude drops by near 50% in both instances. A possible explanation for this is the presence of deformed, thicker ice near the GPRI (small picture in Figure 1a) and mechanical coupling between the floating sea ice and grounded iceberg.

Deleted: The observed wave may thus represent a reflected edge wave and not an onshore wave, which could explain the  $\sim 0.8 \pm 0.2 \text{ mm}$  amplitude (Figure 7c) observed with the GPRI, roughly an order of magnitude lower than with the IWRs. ¶

315 The average observed speed in E1 matches well with the shallow water approximation indicative of an onshore wave. However, the speed appears to increase within  $\sim 70 \text{ m}$  of the GPRI, apparent as a flattening of the curve representing the timing of the wave maximums (Figure 6b). One possible explanation is deflection as the wave approaches the grounded ice giving the appearance of higher speed due to a larger angle between propagation and LOS. Another possible explanation is that the ice in near-range is not in hydrostatic equilibrium, hence reaches its maximum value quicker than when the actual wave crest arrives. A third explanation is that the wave reflects off the grounded ice resulting in a maximum value where the two waves complement each other potentially prior to the arrival of the incoming wave crest. The latter two explanations are based on the fact that the speed is strictly derived from the displacement maximum, which may not represent the wave crest and thus lead to inaccuracies.

Deleted: Figure 5



Formatted: Centered

Figure 10: (a) Derived vertical displacement over 30 seconds on 23 April 2021 at 22:32 UTC (E2). Each line represents one location on the ice where warmer colors signify a closer distance to the radar. The dashed line indicates a linear trend removed for the analysis. (b) Exact time of the trough at different distances from the radar. The red lines indicate average values on each side of the node (c) Amplitude with range with red line indicating the mean.

335 4.2 Uncertainties related to propagation angle and amplitude

The average observed speed in E2 is  $27 \text{ m s}^{-1}$ ,  $17 \text{ m s}^{-1}$  higher than during E1. One possible explanation for this ~~the presence of an edge wave~~ traveling at an angle  $\sim 76^\circ$  from LOS. Although we expect incoming waves to typically orient onshore, such waves can excite waves in ice discontinuities with a conserved period, which will propagate along such boundaries (Marchenko and Semenov, 1994; Marchenko, 1999; Evans and Porter, 2003). We speculate that E2 may ~~incorporate~~ one of these edge

Deleted: is that the wave

Deleted: is in fact

Deleted:  $68^\circ$

Deleted: represent

340 waves generated at the boundary between the refrozen lead and offshore ice (green arrow in Figure 1b). The wave then propagates along this boundary directly up the refrozen lead (pink dashed line in Figure 1b). A second explanation is the stark inhomogeneities in the ice, such as fractures, variable thickness, and rough ice leading to significant reorientation of the wave. InSAR-based snapshots of infragravity wave fields in sea ice indicate that waves fronts can be reoriented by tens of degrees by spatial variations in bathymetry and ice morphology (Mahoney et al., 2016).

345 The wave amplitude in E2 differs from what was observed with the IWRs by an order of magnitude. This is not necessarily surprising as the GPRI was not staring directly at any of the IWRs and satellite-based InSAR observations suggest significant variation in vertical motion (even featuring locations of zero motion) along a single wave front (Mahoney et al., 2016). Hence, in inhomogeneous ice, vertical displacement should be expected to significantly deviate from the average amplitude. Furthermore, if the E2 wave represents a generated edge wave, this may also have resulted in a diminished amplitude value in  
350 addition to attenuation and bathymetric influence on the amplitude. In essence, we do not observe nor expect the amplitude to

355 be conserved in between the well-separated IWRs and the GPRI in the same way as the wave period. The derived amplitude is dependent upon the incidence angle,  $\theta$ , which is subject to uncertainties, predominately driven by inexact estimation of the antenna height atop of the iceberg. Uncertainties from sensor tilt due to iceberg motion are not considered as significant changes in  $\theta$  could be identified in the antenna leveler and interferometric phase as illustrated in the Appendix.

**Deleted:**

#### 4.3 Interpretation constraints due to multiple wave fields and horizontal motion

360 In addition to E1 and E2, there are dozens of different examples of wave-like motion in the GPRI data, but they are typically more difficult to interpret, likely due in part to the presence wave fields with different sources and frequencies. The IWR data suggest that essentially all frequencies in between 0.15-0.02 Hz can occur in the ice and multiple frequencies can be present at one time (Figure 4). The separation of multiple wave signals is challenging due to the short 30 s acquisition window resulting in the predominate capture of partial waves.

**Deleted:** of multiple

**Deleted:** Figure 3

365 In addition to the interpretation challenges from multiple frequency signals, ice displacement in the horizontal plane appears to be the most common limitation for wave interpretation due to frequent horizontal ice motion. The GPRI is more sensitive to horizontal movement than to an equal displacement in the vertical. Hence, even modest lateral motion can complicate wave interpretation. This sensitivity may also enable the GPRI to potentially detect compressional or shear waves from ice-ice interaction propagating in the horizontal plane. However, such waves propagate at speeds on the order of kilometers per second

370 (Rajan et al., 1993) and is expected to result in sharp peaks in displacement that may be difficult to detect. Even though horizontal movement often complicates interpretation, it can typically be identified in a phase signal. This is due to the low vertical sensitivity with range that can lead to implausible values if interpreted as vertical (Dammann et al., 2021b) and the observed identical timing of displacement peaks with range.

## 5 Conclusions

375 This work leverages data from a 2021 coordinated GPRI/IWR campaign to demonstrate and validate the capture of flexural-gravity waves by the two sensors. The GPRI data was captured during modest wave activity  $\sim 1$  mm and less than  $\sim 5\%$  of acquisitions could be used to interpret wave properties due to the presence of what we interpret to be horizontal surface motion and interfering wave fields. We expect this percentage to be larger if data is acquired during larger-amplitude and more persistent wave activity. However, two particularly clear examples analyzed here demonstrate the ability to track even  $\sim 1$  mm 380 wave propagation and properties over a few hundred meters during the absence of secondary motion.

We also expect the collection of longer time series to aid interpretation in the future. In this work we were limited to 30 s of continuous radar acquisitions due to system constraints in stare-mode, specifically the data writing speed of the specific version of the GPRI hardware used here. This limitation does not extend to newer GPRI systems enabling continuous stare-mode acquisitions over hours to potentially days. This will open up possibilities for a more thorough evaluation of the wave signal.

For instance, where we are here limited to look for single “clean” individual waves, we will be able to analyze combinations  
390 of multiple waves and frequencies for instance by applying Fourier analysis.

While the IWRs and similar on-ice installments enable the detection of waves and their properties, the GPRI provides the  
ability to spatially track individual waves. In addition to identifying wave period, speed, and amplitude, it can help provide  
insight into how these properties change over a few hundred meters. This can potentially be used to evaluate ice properties and  
identifying boundaries resulting in different wave propagation. Coordinated IWR/GPRI deployments can be particularly  
395 powerful as it can resolve both regional variability in wave activity as well as the tracking of individual waves in select  
locations. Here, future deployments could attempt to place an IWR directly on the stare line of the GPRI to derive properties  
of the same wave with both sensors to investigate and resolve potential inconsistencies.

While the results discussed here show promise, the acquisition of longer time series and more analysis is required to investigate  
potential applications e.g., determine wave frequencies and amplitudes that can lead to ice fracture and destabilization. For ice  
400 subject to breakout, the GPRI is particularly valuable as it does not require deployment on the ice. Furthermore, the GPRI and  
the IWRs can provide near real-time data not available from other instruments (e.g., moorings) and can potentially aid in the  
development of an early warning system for ice breakout.

**Acknowledgements.** We thank Alexey Marchenko at the University Centre in Svalbard (UNIS) for valuable discussions on  
wave propagation in sea ice. We thank Matthew Druckenmiller at the National Snow and Ice Data Center (NSIDC) for  
405 providing ice thickness data. We are grateful to personnel at Ukpukvik Inupiat Corporation (UIC) Science for logistical  
support.

**Funding.** This work supported by funding from the U.S. Office of Naval Research (award N000141912451) and the U.S.  
Army Corps of Engineers (award W913E521C0004)

**Author contribution.** D.O.D. conducted the interferometric processing and analysis and drafted the initial manuscript. M.A.J.  
410 contributed to all aspects of the analysis and manuscript. A.R.M and E.R.F. designed the field experiment, collected the data  
and provided critical guidance on data interpretation. All co-authors provided valuable recommendations and corrections  
resulting in the final manuscript.

## Appendix

Waves will impact  $\Delta\Phi$  in different ways depending on whether the GPRI is stationed on moving ice or a fixed surface. In the  
415 case of a GPRI placed on floating ice that moves with the waves, the relative vertical displacement,  $d_{vr\text{float}}$ , has an additional  
component due to the vertical motion of the antenna:

$$d_{vr\text{float}}(x, t) = -d_v + A \sin(-\omega t + \varphi_0) \quad (A1)$$

This second term is equivalent to  $d_v$  evaluated at  $x=0$  (red line in Figure A1a). As the waves propagate underneath the GPRI, the antenna will also be subjected to a variable tilt angle,  $\varepsilon$ , depending on the amplitude,  $A$ , and wavelength,  $\lambda_w$ :

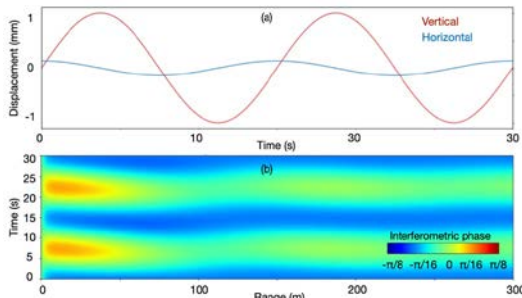
$$420 \quad \varepsilon = -\tan^{-1}\left(\frac{2\pi A}{\lambda_w}\right) \cos(-\omega t + \phi_0) \quad (\text{A2})$$

This will lead to periodic horizontal motion,  $d_{hr\text{float}}$  (blue line in Figure A1a), depending on the elevation of the GPRI antenna,  $h$ :

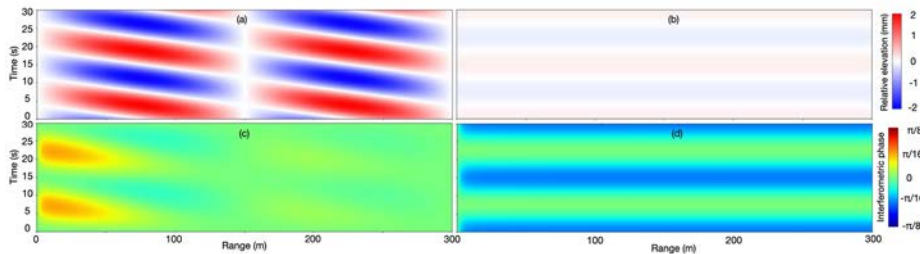
$$d_{hr\text{float}} = -h \sin \varepsilon \quad (\text{A3})$$

The resulting interferogram from both  $d_{vr\text{float}}$  and  $d_{hr\text{float}}$  (Figure A1b) has similarities to interferograms from a fixed system 425 (Figure 2), but are more challenging to interpret (e.g., derive wave speed) due to the added complexity.

To highlight the contributions from vertical and horizontal motion to the phase for a floating GPRI, we isolate the relative vertical motion,  $d_{vr\text{float}}$ , in Figure A2a. At distances equal to multiples of the wavelengths ( $x = n\lambda_w$ ;  $n \in \mathbb{N}$ ), the GPRI and the ice surface will move in phase leading to nodes where  $d_{vr\text{float}} = 0$  (Figure A2a). Halfway between these nodes ( $x = (n + \frac{1}{2})\lambda_w$ ), the GPRI and ice surface will move out of phase leading to a maximum relative vertical displacement twice 430 that of the wave amplitude. Similarly, we isolate the much smaller periodic horizontal motion,  $d_{hr\text{float}}$ , component in (Figure A2b). The resulting interferogram from  $d_{vr\text{float}}$  exhibits a predominate near-range phase response, while the interferogram due to  $d_{hr\text{float}}$  exhibit a phase contribution nearly independent of range (Figure A2c and A2d respectively). The effect of Figure A2c and d results in the interferogram in Figure A1b.



435 **Figure A1:** (a) Simulated vertical (red) and horizontal (blue) GPRI antenna motion as a result of waves ( $T = 15$  s,  $A = 1$  mm,  $\lambda_w = 150$  m,  $h = 2$  m). (b) Simulated interferogram of a floating GPRI system based on a propagating wave including antenna motion in (a).



440 **Figure A2:** Relative change in vertical (a) and horizontal (b) distance between the GPRI antenna and the ice surface due to the wave  
in Figure A1. The resulting interferograms from the isolated motion in a and b (c and d respectively).

## References

445 Ardhuin, F., Collard, F., Chapron, B., Girard-Ardhuin, F., Guitton, G., Mouche, A., and Stopa, J. E.: Estimates of ocean wave heights and  
attenuation in sea ice using the SAR wave mode on Sentinel-1A, *Geophys Res Lett*, 42, 2317-2325, 2015.  
Ardhuin, F., Stopa, J., Chapron, B., Collard, F., Smith, M., Thomson, J., Doble, M., Blomquist, B., Persson, O., and Collins III, C. O.:  
Measuring ocean waves in sea ice using SAR imagery: A quasi-deterministic approach evaluated with Sentinel-1 and in situ data, *Remote  
Sens Environ*, 189, 211-222, 2017.  
450 Crocker, G., and Wadhams, P.: Observations of wind-generated waves in Antarctic fast ice, *Journal of physical oceanography*, 18, 1292-  
1299, 1988.  
Czipott, P. V., and Podney, W. N.: Measurement of fluctuations in the tilt of Arctic ice at the Cearex Oceanography Camp: Experiment  
review, data catalog and preliminary results, PHYSICAL DYNAMICS INC LA JOLLA CA, 1989.  
455 Dammann, D. O., Johnson, M. A., Fedders, E., Mahoney, A., Werner, C., Polashenski, C. M., Meyer, F., and Hutchings, J. K.: Ground-  
based radar interferometry of sea ice, *Remote Sensing*, 13(1), 10.3390/rs13010043, 2021a.  
Dammann, D. O., Mahoney, A., Johnson, M., Eicken, H., Eriksson, L. E. B., Meyer, F., Fedders, E., and Fahnestock, M.: Applications of  
460 radar interferometry for measuring ice motion, *Proceedings of the 26 th International Conference on Port and Ocean Engineering under  
Arctic Conditions*, Moscow, Russia, 2021b  
Dammann, D. O., Johnson, M. A., Mahoney, A., Fedders, E., Ito, M., Hutchings, J. K., Polashenski, C. M., and Fahnestock, M.: Ground-  
based radar interferometry for monitoring landfast sea ice dynamics, *Cold Reg Sci Technol*, 10.3390/rs13010043, in review.  
465 Doble, M., Mercer, D. J., Meldrum, D., and Peppe, O. C.: Wave measurements on sea ice: developments in instrumentation, *Annals of  
Glaciology*, 44, 108-112, 2006.  
Druckenmiller, M. L., Eicken, H., George, J. C., and Brower, L.: Trails to the whale: reflections of change and choice on an Inupiat  
icescape at Barrow, Alaska, *Polar Geography*, 36, 5-29, 10.1080/1088937X.2012.724459, 2013.  
Evans, D., and Porter, R.: Wave scattering by narrow cracks in ice sheets floating on water of finite depth, *Journal of fluid Mechanics*, 484,  
470 143-165, 2003.  
Horvat, C., Blanchard-Wrigglesworth, E., and Petty, A.: Observing waves in sea ice with ICESat-2, *Geophys Res Lett*, 47,  
e2020GL087629, 2020.  
Johnson, M., Mahoney, A., Sybrandy, A., and Montgomery, G.: Measuring acceleration and short-lived motion in landfast sea-ice, *Journal  
of Ocean Technology*, 15, 2020.  
475 Johnson, M. A., Marchenko, A. V., Damann, D. O., and Mahoney, A. R.: Observing Wind-Forced Flexural-Gravity Waves in the  
Beaufort Sea and Their Relationship to Sea Ice Mechanics, *Journal of Marine Science and Engineering*, 9, 471, 2021.  
Kohout, A. L., Penrose, B., Penrose, S., and Williams, M. J.: A device for measuring wave-induced motion of ice floes in the Antarctic  
marginal ice zone, *Annals of Glaciology*, 56, 415-424, 2015.  
Kovalev, D. P., Kovalev, P. D., and Squire, V. A.: Crack formation and breakout of shore fast sea ice in Mordvinova Bay, south-east  
Sakhalin Island, *Cold Reg Sci Technol*, 175, 103082, 2020.  
Kovalev, P. D., and Squire, V. A.: Ocean wave/sea ice interactions in the south-eastern coastal zone of Sakhalin Island, *Estuarine, Coastal  
and Shelf Science*, 238, 106725, 2020.

Mahoney, A., Dammann, D. O., Johnson, M. A., Eicken, H., and Meyer, F. J.: Measurement and imaging of infragravity waves in sea ice using InSAR, *Geophys Res Lett*, 43, 6383–6392, 10.1002/2016GL069583 2016.

480 Marchenko, A., and Semenov, A. Y.: Edge waves in a shallow fluid beneath a fractured elastic plate, *Fluid dynamics*, 29, 589-592, 1994.

Marchenko, A.: Parametric excitation of flexural-gravity edge waves in the fluid beneath an elastic ice sheet with a crack, *European Journal of Mechanics-B/Fluids*, 18, 511-525, 1999.

Rabault, J., Sutherland, G., Gundersen, O., Jensen, A., Marchenko, A., and Breivik, Ø.: An open source, versatile, affordable waves in ice instrument for scientific measurements in the Polar Regions, *Cold Reg Sci Technol*, 170, 102955, 2020.

485 Rajan, S. D., Frisk, G. V., Doutt, J. A., and Sellers, C. J.: Determination of compressional wave and shear wave speed profiles in sea ice by crosshole tomography—Theory and experiment, *The Journal of the Acoustical Society of America*, 93, 721-738, 1993.

Smith, M., and Thomson, J.: Pancake sea ice kinematics and dynamics using shipboard stereo video, *Annals of Glaciology*, 61, 1-11, 2020.

Squire, V. A.: An investigation into the use of strain rosettes for the measurement of propagating cyclic strains, *Journal of Glaciology*, 20, 425-431, 1978.

490 Squire, V. A., Dugan, J. P., Wadhams, P., Rottier, P. J., and Liu, A. K.: Of ocean waves and sea ice, *Annual Review of Fluid Mechanics*, 27, 115-168, 1995.

Squire, V. A.: Of ocean waves and sea-ice revisited, *Cold Reg Sci Technol*, 49, 110-133, 2007.

Squire, V. A.: A fresh look at how ocean waves and sea ice interact, *Philosophical Transactions of the Royal Society A: Mathematical, Physical and Engineering Sciences*, 376, 20170342, 2018.

495 Sutherland, G., and Rabault, J.: Observations of wave dispersion and attenuation in landfast ice, *Journal of Geophysical Research: Oceans*, 121, 1984-1997, 2016.

Sutherland, P., Brozena, J., Rogers, W. E., Doble, M., and Wadhams, P.: Airborne remote sensing of wave propagation in the marginal ice zone, *Journal of Geophysical Research: Oceans*, 123, 4132-4152, 2018.

Thomson, J., and Rogers, W. E.: Swell and sea in the emerging Arctic Ocean, *Geophys Res Lett*, 41, 3136-3140, 2014.

500 Thomson, J., Gemmrich, J., Rogers, W. E., Collins, C. O., and Arduhui, F.: Wave groups observed in pancake sea ice, *Journal of Geophysical Research: Oceans*, 124, 7400-7411, 2019.

Yadav, J., Kumar, A., and Mohan, R.: Dramatic decline of Arctic sea ice linked to global warming, *Natural Hazards*, 103, 2617-2621, 2020.